Mixed Sr and Ba Tri-Stannides/Plumbides $A^{II}(Sn_{1-x}Pb_x)_3$

Michael Langenmaier [†,‡], **Michael Jehle** [†,‡] **and Caroline Röhr** *

Institut für Anorganische und Analytische Chemie, Albert-Ludwigs-Universität Freiburg, 79104 Freiburg, Germany; michil@limonite.chemie.uni-freiburg.de (M.L.); michij@almandine.chemie.uni-freiburg.de (M.J.)

* Correspondence: caroline@ruby.chemie.uni-freiburg.de; Tel.: +49-0761-203-6143

† These authors contributed equally to this work.

‡ Institut für Anorganische und Analytische Chemie, Albert-Ludwigs-Universität Freiburg, Albertstr. 21, D-79104 Freiburg, Germany.

Abstract: The continuous substitution of tin by lead (M^{IV}) allows for the exploration geometric criteria for the stability of the different stacking variants of alkaline-earth tri-tetrelides $A^{II}M_3^{IV}$. A series of ternary Sr and Ba mixed tri-stannides/plumbides $A^{II}(Sn_{1-x}Pb_x)_3$ (A^{II} = Sr, Ba) was synthesized from stoichiometric mixtures of the elements. Their structures were determined by means of single crystal X-ray data. All structures exhibit close packed ordered AM_3 layers containing M kagomé nets. Depending on the stacking sequence, the resulting M polyanion resembles the oxygen substructure of the hexagonal (face-sharing octahedra, h stacking, Ni_3Sn-type, border compound $BaSn_3$) or the cubic (corner-sharing octahedra, c stacking, Cu_3Au-type, border compound $SrPb_3$) perovskite. In the binary compound $BaSn_3$ (Ni_3Sn-type) up to 28% of Sn can be substituted against Pb ($hP8$, $P6_3/mmc$, $x = 0.28(4)$: $a = 726.12(6)$, $c = 556.51(6)$ pm, $R1 = 0.0264$). A further increased lead content of 47 to 66% causes the formation of the $BaSn_{2.57}Bi_{0.43}$-type structure with a $(hhhc)_2$ stacking [$hP32$, $P6_3/mmc$, $x = 0.47(3)$: $a = 726.80(3)$, $c = 2235.78(14)$ pm, $R1 = 0.0437$]. The stability range of the $BaPb_3$-type sequence $(hhc)_3$ starts at a lead proportion of 78% ($hR36$, $R\bar{3}m$, $a = 728.77(3)$, $c = 2540.59(15)$ pm, $R1 = 0.0660$) and reaches up to the pure plumbide $BaPb_3$. A second new polymorph of $BaPb_3$ forms the Mg_3In-type structure with a further increased amount of cubic sequences [$(hhcc)_3$; $hR48$, $a = 728.7(2)$, $c = 3420.3(10)$ pm, $R1 = 0.0669$] and is thus isotypic with the border phase $SrSn_3$ of the respective strontium series. For the latter, a Pb content of 32% causes a small existence region of the $PuAl_3$-type structure [$hP24$, $P6_3/mmc$, $a = 696.97(6)$, $c = 1675.5(2)$ pm, $R1 = 0.1182$] with a $(hcc)_2$ stacking. The series is terminated by the pure c stacking of $SrPb_3$, the stability range of this structure type starts at 75% Pb ($cP4$, $Pm\bar{3}m$; $a = 495.46(9)$ pm, $R1 = 0.0498$). The stacking of the close packed layers is evidently determined by the ratio of the atomic radii of the contributing elements. The Sn/Pb distribution inside the polyanion ('coloring') is likewise determined by size criteria. The electronic stability ranges, which are discussed on the basis of the results of FP-LAPW band structure calculations are compared with the *Zintl* concept and *Wade*'s/*mno* electron counting rules. Still, due to the presence of only partially occupied steep M-p bands the compounds are metals exhibiting pseudo band gaps close to the Fermi level. Thus, this structure family represents an instructive case for the transition from polar ionic/covalent towards (inter)metallic chemistry.

Keywords: stannides; plumbides; alkaline-earth

1. Introduction

In view of the complex bonding situation between ionic, covalent and metallic, the synthetic, crystallographic and bond theoretical studies on geometric and electronic parameters determining

the structure chemistry (and therewith also the properties) of polar intermetallics of the alkali and alkaline-earth compounds of the *p*-block elements are still a fascinating field of research. Compared to the vast number of alkali/alkaline-earth stannides and plumbides [1], which are simple electron-precise *Zintl* phases, the tri-stannides and -plumbides ASn_3 and APb_3 of the alkaline-earth elements (A = Ca, Sr, Ba) are ordered derivatives of simple dense packings of the two elements [2–9]. Similar to the variation of the alkaline-earth elements (A) in the pure tri-stannides [10] and tri-plumbides [11], a continuous substitution of tin by lead allows for the exploration of geometric and electronic (Sn/Pb distribution) criteria for the stability of different stacking variants of the hexagonal close packed layers [AM_3] in these tri-tetrelides $A^{II}M^{IV}_3$.

The tri-plumbides APb_3 of calcium and strontium, which both form the cubic Cu_3Au-type structure (|:ABC:| or *c* stacking after *Jagodzinski*), have been structurally characterized using X-ray powder data in the past and some physical properties as well as the electronic band structure were reported in the 1960s and 1970s by Havinga et al. [6,12,13]. More recent works on their electronic and magnetic properties were published by Baranovskiy et al. [14,15]. The structure of the binary barium plumbide $BaPb_3$ [$(hhc)_3$ stacking] was derived and refined from 78 reflections by *Sands*, *Wood* and *Ramsey* as early as 1964 [9]. Only two years later, *van Vucht* published an elaborate work [7], in which he, based on powder diffraction data, already suggested the existence of further stacking variants for the mixed alkaline-earth plumbides $A_xBa_{1-x}Pb_3$ (A = Ca, Sr). These two series have been fully explored by our group 10 years ago [11]: Both the Ca and the Sr series start with the pure *c* stacking of (Ca/Sr)Pb$_3$. At an approximate 1:1 ratio of strontium and barium (e.g., 35 to 53% Sr) the $PuAl_3$-type [$(hcc)_2$ stacking] has a distinct homogeneity range. Reversely, the $(hhc)_3$ stacking of the binary compound $BaPb_3$ changes at an already very small partial substitution of barium against calcium ($Ca_{0.03}Ba_{0.97}Pb_3$) or strontium ($Sr_{0.11}Ba_{0.89}Pb_3$) towards the $(hhcc)_3$ sequence of the Mg_3In-type.

For the tri-stannides ASn_3, the continuous substitution of the different alkaline-earth cations against each other has been likewise investigated in a systematic study [10]: Starting from $CaSn_3$ (pure *c* stacking [2]) up to 46% of Ca can be substituted against Sr without a structural change. The binary phase $SrSn_3$ forms the Mg_3In-type structure with a $(hhcc)_3$ stacking sequence [3]. A small partial substitution of Sr against Ba (9 to 19%) causes the packing to switch to the $(hhc)_3$ sequence of the $BaPb_3$-type. At a Ba proportion of 26% a further structure change to the $BaSn_{2.57}Bi_{0.43}$-type structure [$(hhhc)_2$ stacking] takes place. The tin series terminates with the pure *h* stacking of $BaSn_3$; the stability range of this Ni_3Sn-type structure starts at the composition $Sr_{0.22}Ba_{0.78}Sn_3$.

Beyond these pure geometric/size effects, *van Vucht* and *Havinga* [8,16] also demonstrated the electronic influence on the *h*/*c* stacking of the layers in several Tl-substituted plumbides $A(Tl/Pb)_3$. An indium content in $Ba(In/Pb)_3$ of 15% also changes the stacking from the simple cubic to the mixed $(hcc)_2$ sequence of the $PuAl_3$-type [17]. For the electron-richer system $BaSn_3$–$BaBi_3$ a similar influence of the valence electron (v.e.) number on the stacking was shown more recently by Fässler et al. [18].

In the present work, we report on the results of a systematic experimental, crystallographic and bond-theoretical DFT investigation of mixed Sn/Pb tri-tetrelides of Sr and Ba. Here, the substitution of tin by lead does not only change the geometric relations, but in addition the occupation of the crystallographically different *M* positions of the more complex stacked sequences with tin and/or lead, i.e., the 'coloring' of the polyanion [19] can be studied.

2. Experimental

2.1. Synthesis and Phase Widths

The synthesis of the mixed Sn/Pb tri-tetrelides was generally performed starting from the elements strontium or barium, tin and lead as obtained from commercial sources (Sr, Ba: Metallhandelsgesellschaft Maassen, Bonn, 99%; Sn: shots, 99.9%, Riedel de Häen; Pb: powder, 99.9%, Merck KGaA). The elements were filled into tantalum crucibles in a glovebox under an argon atmosphere and the sealed containers were heated up with a rate of 200 °C/h to maximum

temperatures (T_{max}) of 700 to 800 °C. For all samples, the crystallization was performed by a slow cooling rate ($\dot{T}^{\downarrow}$) of 2 to 20 °C/h. The maximum temperatures applied and the detailed cooling rates can be found in Table 1, together with the weighed sample compositions, which were mainly restricted to the stoichiometric 1:3 [for (Sr/Ba):(Sn/Pb)] element ratio. All sample reguli were hard and brittle with a dark-metallic luster and are sensitive against moisture. Representative parts of the reguli were ground and sealed in capillaries with a diameter of 0.3 mm. X-ray powder patterns were collected on transmission powder diffraction systems (STADI-P or Dectris Mythen 1K detector, Stoe & Cie, Darmstadt, MoK_α radiation, graphite monochromator). For the phase analysis, the measured powder patterns were compared to the calculated (program LAZY-PULVERIX [20]) reflections of the title compounds and other known phases in the respective ternary systems.

Table 1. Details of the synthesis of the title compounds (cf. Tables 2 and 3 for the single crystal numbers; uniform heating rate: $\dot{T}^{\uparrow}$ = 200 °C/h) .

Sample	Structure	Single	Pb	Weighed Elements						Temperature Program					
Composition	Type	Crystal	Content	Sr/Ba		Sn		Pb		T_{max}	$\dot{T}^{\downarrow}$	T	$\dot{T}^{\downarrow}$	T	$\dot{T}^{\downarrow}$
		No.	[%]	[mg]	[mmol]	[mg]	[mmol]	[mg]	[mmol]	(in [°C] and [°C/h])					
BaSn$_2$Pb	Ni$_3$Sn	**1**	28	253.7	1.85	407.0	3.43	356.8	1.72	750	30	500	200		
BaSn$_{1.5}$Pb$_{1.5}$	BaSn$_{2.6}$Bi$_{0.4}$	**2**	47.4	220.7	1.61	284.7	2.40	496.7	2.40	750	200	650	2	500	200
BaSnPb$_2$	BaSn$_{2.6}$Bi$_{0.4}$	**3**	66.3	205.2	1.49	176.0	1.48	619.4	2.99	750	20	500	200		
BaSn$_{0.75}$Pb$_{2.25}$	BaPb$_3$	**4**	78.3	199.6	1.45	129.1	1.09	675.9	3.26	750	200	650	2	500	200
BaSn$_{0.5}$Pb$_{2.5}$	BaPb$_3$	**4p**	85	192.2	1.40	88.1	0.74	724.3	3.50	750	30	500	200		
BaGePb$_2$	Mg$_3$In	**5**	100	220.6	1.61	116.9	1.61	663.6	3.20	750	30	500	200		
SrSn$_{2.5}$Pb$_{0.5}$	Mg$_3$In	**5p**	14	179.7	2.05	608.8	5.13	212.3	1.02	800	200	750	2	625	200
SrSn$_2$Pb	PuAl$_3$	**6**	32	164.8	1.88	445.5	3.75	389.6	1.88	800	200	750	2	625	200
SrSn$_{1.5}$Pb$_{1.5}$	PuAl$_3$	**6p**	34	152.0	1.73	307.9	2.59	539.0	2.60	700	20	500	200		
SrSn$_{0.75}$Pb$_{2.25}$	Cu$_3$Au	**7**	75	137.1	1.56	138.7	1.17	726.0	3.50	700	20	500	200		

Starting from the pure tin compound, the first ternary sample of the <u>Ba series</u>, with an overall composition of BaSn$_2$Pb, yielded the border phase BaSn$_{2.16}$Pb$_{0.84}$ (**1**) of the Ni$_3$Sn-type (magenta bar in Figure 1) in pure phase. The powder pattern of the samples with a Pb content of 50% and 66.7% could be fully indexed with the data of the BaSn$_{2.6}$Bi$_{0.4}$-type. Accordingly, the two border phases of the existence range of this structure type (dark blue bar in Figure 1), BaSn$_{1.58}$Pb$_{1.42}$ (**2**) and BaSn$_{1.01}$Pb$_{1.99}$ (**3**), were obtained from these two samples. The following two samples with a further increased lead content, BaSn$_{0.75}$Pb$_{2.25}$ and BaSn$_{0.5}$Pb$_{2.5}$, yielded ternary Sn-containing variants of the known BaPb$_3$-type structure (cyan). The refined chemical composition of the border phase obtained from the first sample, BaSn$_{0.65}$Pb$_{2.35}$ (**4**), is very close to the weighed sample stoichiometry, the composition of the somewhat Pb-richer phase was refined from powder data. A second form of BaPb$_3$, which is isostructural to SrSn$_3$ (green bar in Figure 1), was obtained for the first time from the Ge-containing sample (BaGePb$_2$), which contains (optically visible) elemental germanium as a second product. In the Sr series, a lead content of 17% (SrSn$_{2.5}$Pb$_{0.5}$) still yielded the Mg$_3$In-type structure of the binary tri-stannide SrSn$_3$. The composition of this phase (SrSn$_{2.58}$Pb$_{0.42}$) was refined from powder data (Section 2.3). The two samples with an Sn-content of 66 and 50% contain PuAl$_3$-type phases. For the first sample, the single crystal data of selected crystals are in very good agreement with the weighed element ratio (**6**: SrSn$_{2.05}$Pb$_{0.95}$, Section 2.2). Due to the low crystal quality, the composition of the Pb-richer phase of this type could be only refined from powder data (Section 2.3). A small content of the Pb-richer cubic Cu$_3$Au-type phase, which is formed in X-ray pure form in the final sample SrSn$_{0.75}$Pb$_{2.25}$, could not be excluded due to the overlap of the few reflections of the Cu$_3$Au-type with those of the structurally related PuAl$_3$-type.

2.2. Single Crystal Structure Refinements

For the crystal structure refinements (cf. Tables 2 and 3), irregularly shaped single crystals were selected using a stereo microscope and mounted in glass capillaries (diameter 0.1 mm) under dried

paraffine oil. The crystals were centered on diffractometers equipped with an image plate (Stoe IPDS, sealed tube) or a CCD detector (Bruker Apex-II Quazar, microfocus source).

Table 2. Crystallographic data and details of the data collection and structure refinement of the compounds of the barium series $BaSn_{2.16}Pb_{0.84}$ (**1**), $BaSn_{1.58}Pb_{1.42}$ (**2**), $BaSn_{1.01}Pb_{1.99}$ (**3**), $BaSn_{0.65}Pb_{2.35}$ (**4**), and $BaPb_3$ (**5**) and the strontium compounds $SrSn_{2.05}Pb_{0.95}$ (**6**) and $SrSn_{0.75}Pb_{2.25}$ (**7**).

A^{II} ⊢		Ba Compounds					⊣ ⊢ Sr Compounds ⊣	
No.		**1**	**2**	**3**	**4**	**5**	**6**	**7**
Pb content, %		28	47.4	66.3	78.3	100	32	75
Structure type		Ni_3Sn ⊢	$BaSn_{2.6}Bi_{0.4}$	⊣	$BaPb_3$	Mg_3In	$PuAl_3$	Cu_3Au
Stacking sequence		h_2 ⊢	$(hhhc)_2$	⊣	$(hhc)_3$	$(hhcc)_3$	$(hcc)_2$	c_3
Crystal system	⊢		hexagonal		⊣ ⊢	rhombohedric	⊣ hexagonal	cubic
Space group	⊢		$P6_3/mmc$		⊣ ⊢	$R\bar{3}m$	⊣ $P6_3/mmc$	$Pm\bar{3}m$
	⊢		no. 194		⊣ ⊢	no. 166	⊣ no. 194	no. 221
Pearson symbol		$hP8$ ⊢		$hP32$	⊣ ⊢	$hR36$	⊣ $hR48$	$cP4$
Lattice parameters, pm	a	726.12(6)	726.80(3)	728.12(4)	728.77(3)	728.7(2)	696.97(6)	495.46(9)
	c	556.51(6)	2235.78(14)	2254.81(13)	2540.6(2)	3420.3(12)	1675.5(2)	
Volume of the u.c., 10^6 pm^3		254.11(5)	1022.80(11)	1035.25(13)	1168.55(12)	1572.8(11)	704.87(15)	
Volume/f.u., 10^6 pm^3		127.06	127.85	129.41	129.84	131.07	117.49	121.63(7)
c/a		1.5328	1.5380	1.5484	1.5494	1.5646	1.6027	1.63
Z		2	8	8	9	12	6	1
Density (X-ray), gcm^{-3}		7.38	8.04	8.59	8.97	9.62	7.46	8.78
Diffractometer	⊢		Stoe IPDS-II		⊣ ⊢		APEX-II	⊣
	⊢			Mo-K_α radiation				⊣
Absorption coefficient $\mu_{Mo-K\alpha}$, mm^{-1}		44.7	61.7	76.6	86.2	103.3	55.7	92.1
`range, deg		3.2–29.1	1.8–29.3	1.8–29.3	2.4–29.1	1.8–30.0	3.4–29.9	4.1–32.5
No. of reflections collected		3737	7730	9690	5106	5074	6364	730
No. of independent reflections		155	582	593	431	628	433	69
R_{int}		0.0723	0.0732	0.1072	0.2342	0.1131	0.1023	0.0860
Corrections	⊢		Lorentz, Polarisation, Absorption					⊣
	⊢		XShape [21]		⊣ ⊢		Sadabs [22]	⊣
Structure refinement	⊢			SHELXL-2013 [23]				⊣
No. of free parameter		9	25	25	18	20	18	6
Goodness-of-fit on F^2		1.248	1.372	1.383	1.116	0.969	1.243	1.263
R Values [for refl. with $I \geq 2\sigma(I)$]	$R1$	0.0264	0.0437	0.0423	0.0660	0.0499	0.1182	0.0571
	$wR2$	0.0644	0.0934	0.0566	0.1738	0.1166	0.3585	0.1610
R Values (all data)	$R1$	0.0266	0.0485	0.0506	0.0683	0.0772	0.1270	0.0572
	$wR2$	0.0644	0.0948	0.0578	0.1761	0.1258	0.3642	0.1610
Residual elect. density, e$^-$ $\times 10^{-6}$ pm^{-3}		+1.2/−1.5	+2.2/−1.8	+2.7/−1.8	+5.6/−1.9	+6.4/−3.1	+9.8/−3.7	+7.4/−4.0

The reflections of the tin-rich compounds of the Ba series could be indexed by the expected small hexagonal cell of the Ni_3Sn type (space group $P6_3/mmc$). The border compound of the stability range of this structure type, $BaSn_{2.16}Pb_{0.84}$ (**1**), was obtained in pure phase from a sample of overall composition $BaSn_2Pb$. The parameters of the structure model of the pure tri-stannide [5] were refined using the program SHELXL-2013 [23], and the mixed Sn/Pb position was treated with constrained positional and anisotropic displacement parameters (ADPs). The obtained formula $BaSn_{2.16}Pb_{0.84}$ is only slightly Sn-richer than the sample composition. Crystals yielded from the lead-richer samples $BaSn_{1.58}Pb_{1.42}$ and $BaSn_{1.01}Pb_{1.99}$ show a similar hexagonal basis and the same extinction conditions, but the length of the hexagonal c axis increases to about 2200 pm, which indicates the formation of the $BaSn_{2.6}Bi_{0.4}$-type structure [18]. The two border compounds of the stability range of this structure type contain 47.4 (**2**) and 66.3% (**3**) lead, which is again close to the respective sample compositions. Accordingly, the powder patterns of these two samples are fully indexed with the data of the $BaSn_{2.6}Bi_{0.4}$-type.

Table 3. Atomic coordinates and equivalent isotropic displacement parameters (pm^2) for the single crystal structures of the title compounds.

Compound	No.	Atoms	Wyckoff Position	Point Group Symmetry	Stacking Sequence	Pb Prop. /%	x	y	z	$U_{equiv.}$
BaSn$_{2.16}$Pb$_{0.84}$	**1**	Ba	2*d*	$\bar{6}m2$			1/3	2/3	3/4	263(6)
		M	6*h*	*mm*2	*h*	28.0(14)	0.14395(7)	2*x*	1/4	244(4)
BaSn$_{1.58}$Pb$_{1.42}$	**2**	Ba(1)	2*a*	$\bar{3}m$.			0	0	0	250(6)
		Ba(2)	2*b*	$\bar{6}m2$			0	0	1/4	201(5)
		Ba(3)	4*f*	3*m*.			1/3	2/3	0.13534(8)	176(4)
		M(1)	6*h*	*mm*2	*h*	9.5(13)	0.52781(12)	2*x*	1/4	202(6)
		M(2)	12*k*	.*m*.	*h*	40.1(12)	0.18965(8)	2*x*	0.62443(4)	227(4)
		Pb(3)	6*g*	$.\frac{2}{m}.$	*c*		1/2	0	0	266(3)
BaSn$_{1.01}$Pb$_{1.99}$	**3**	Ba(1)	2*a*	$\bar{3}m$.			0	0	0	268(5)
		Ba(2)	2*b*	$\bar{6}m2$			0	0	1/4	211(5)
		Ba(3)	4*f*	3*m*.			1/3	2/3	0.13465(6)	189(3)
		M(1)	6*h*	*mm*2	*h*	23.7(1)	0.52645(9)	2*x*	1/4	210(4)
		M(2)	12*k*	.*m*.	*h*	70.6(9)	0.18753(5)	2*x*	0.62418(3)	232(2)
		Pb(3)	6*g*	$.\frac{2}{m}.$	*c*		1/2	0	0	262(2)
BaSn$_{0.65}$Pb$_{2.35}$	**4**	Ba(1)	3*a*	$\bar{3}m$			0	0	0	374(9)
		Ba(2)	6*c*	3*m*			0	0	0.21602(10)	324(7)
		M(1)	18*h*	.*m*	*h*	67(2)	0.47707(12)	−*x*	0.22315(4)	364(6)
		Pb(2)	9*e*	$.\frac{2}{m}$	*c*		1/2	0	0	388(6)
BaPb$_3$	**5**	Ba(1)	6*c*	3*m*			0	0	0.13034(7)	220(5)
		Ba(2)	6*c*	3*m*			0	0	0.28912(7)	234(5)
		Pb(1)	18*h*	.*m*	*h*		0.47742(8)	−*x*	0.12358(3)	252(3)
		Pb(2)	18*h*	.*m*	*c*		0.50625(8)	−*x*	0.29199(3)	297(3)
SrSn$_{2.05}$Pb$_{0.95}$	**6**	Sr(1)	2*b*	$\bar{6}m2$			0	0	1/4	180(20)
		Sr(2)	4*f*	3*m*.			1/3	2/3	0.0930(5)	185(18)
		Sn(1)	6*h*	*mm*2	*h*		0.5218(4)	0.0436(8)	1/4	182(15)
		M(2)	12*k*	.*m*.	*c*	47(4)	0.16833(19)	0.3367(4)	0.58108(13)	221(11)
SrSn$_{0.75}$Pb$_{2.25}$	**7**	Sr	1*a*	$m\bar{3}m$			0	0	0	500(20)
		M	3*c*	$\frac{4}{m}m.m$	*c*	75	0	1/2	1/2	159(9)

The diffraction images of the crystals obtained from the Pb-rich sample BaSn$_{0.5}$Pb$_{2.5}$ could be indexed by a rhombohedral lattice with the familiar unit cell basis of 730 pm, but now with a *c* axis of ≈2500 pm, which indicates the formation of the BaPb$_3$-type structure. During the single crystal refinement of this structure model, the 18*h* position *M*(1) turned out to be statistically occupied by tin and the final refinement yielded a Sn occupation of 67(2)%, i.e., an overall composition of BaSn$_{0.65}$Pb$_{2.35}$ (**4**), which is again close to the weighed element ratios. For the likewise rhombohedral unit cell of the second form of BaPb$_3$-II (**5**), the large *c* axis indicated the 12-layer structure of the Mg$_3$In-type, which was also found for ternary derivatives of BaPb$_3$ containing small amounts of Ca or Sr [11]. The structure refinement converged to *R*1 values of 0.05 and the refinement as well as the unit cell volume (cf. the comparison in Section 3.1.4) gave no indication for an incorporation of germanium into the structure. All crystals of the Sr-series were of much lower quality than those of the Ba compounds and the diffraction images of crystals of different sizes all exhibit very broad reflections. Only the structure of the compound **6** (SrSn$_{2.05}$Pb$_{0.95}$), which forms the hexagonal PuAl$_3$-type, could be refined from single crystal data. However, a quite large value of *R*1 and the residual electron density of about +10 e$^-$10^{-6} pm^{-3}, which lies in the vicinity of the *M*(2) position, result from the unsatisfactory quality of the diffraction data. In the case of the single crystals yielded from the sample SrSn$_{0.75}$Pb$_{2.25}$ (**7**) the situation is even worse, and the Sn:Pb ratio of the sole *M* position in the cubic Cu$_3$Au-type structure had to be fixed to the weighed element ratio.

The data of the single crystal structure refinements, in which the *M* sites are sorted according to increasing lead content (Table 3) and all atomic parameters were transformed to a standardized setting according to STRUCTURE TIDY [24], have been deposited [25].

2.3. Rietveld Refinements

The X-ray powder data used for the full-pattern *Rietveld* refinements were collected on the above mentioned powder diffractometer (Dectris Mythen 1K detector) in the 2Θ range 2 to 41.8° with a step width of 1.17° and an exposure time of 180 s/step. The *Rietveld* refinements were performed using the programs GSAS [26] and EXPGUI [27].

The powder pattern of the sample $SrPb_{0.5}Sn_{2.5}$ (**5p**) could be fully indexed and refined starting from the crystal data of $SrSn_3$ (Mg_3In-type [28]). The obtained lattice parameters (a = 696.50(6), c = 3324.9(5) pm, V/f.u. = 116.4 × 10^6 pm^3), which are somewhat larger than those of the binary compound $SrSn_3$ (a = 694.0, c = 3301.0 pm [3]) already indicated a small lead content. The refinement of the Sn/Pb ratio of the $M(2)$ position (R_P = 0.0611, wR_P = 0.0876) resulted in 28(1)% lead for this site and an overall composition of $SrPb_{0.42}Sn_{2.58}$, which is in good agreement with the weighed sample composition.

For the *Rietveld* refinement of the structure of the phase obtained from the sample $SrPb_{0.95}Sn_{2.05}$ (**6p**), the model of the $PuAl_3$-type, which allowed the full indexing of the powder pattern, was used. The lattice parameters converged at a = 701.06(1) and c = 1683.29(5) pm (V/f.u. = 119.4 × 10^6 pm^3; R_P = 0.0212, wR_P = 0.0270 and R_{F2} = 0.0580). The statistical Sn:Pb ratio of the $M(2)$ position could be refined to 38(1):62(1)%, which is slightly Pb-richer than the relation of the single crystal refinements of **6** ($SrSn_{2.05}Pb_{0.95}$). Accordingly, the lattice parameters are somewhat increased.

2.4. Band Structure Calculations

DFT calculations of the electronic band structure were performed for the border phases of the compound series, $BaSn_3$ and $SrPb_3$, as well as for the two polymorphs of $BaPb_3$ and for $SrSn_3$ using the FP-LAPW method (programs WIEN2K [29] and ELK [30], cf. Table 4). Herein, the exchange-correlation contribution was described by the *Generalized Gradient Approximation* (GGA) of *Perdew*, *Burke* and *Ernzerhof* [31]. Muffin-tin radii were chosen as 121.7 pm (2.3 a.u.) for all atoms. Cutoff energies used are E_{max}^{pot} = 190 eV (potential) and E_{max}^{wf} = 170 eV (interstitial PW). Further parameters (e.g., number of k points) and selected results of the calculations are collected in Table 4. Electron densities, the *electron localisation function* (ELF) [32,33] and *Fermi* surfaces were visualized using the programs XCRYSDEN [34] and DRAWXTL [35]. A *Bader* 'atoms in molecules' (AIM) analysis of the electron density map was performed to evaluate the charge distribution between the atoms and the heights and positions of the bond, ring and cage critical points [36] using the program CRITIC2 [37,38]. The total DOS (tDOS) plots of all compounds are discussed in Section 3.5.2. For the two border compounds of the series, $BaSn_3$ and $SrPb_3$, plots of the partial DOS (pDOS) and the band structures themselves are already reported elsewhere [3,10,11,14]. Maps of the ELF of $SrSn_3$ based on LMTO-ASA calculations by *Fässler* et al. [3] are in very good agreement with the ELF obtained herein.

Both the band structures and the ELF of the binary compounds reported in the literature are considered in the discussion on the chemical bonding in Section 3.5.2.

Table 4. Details of the calculation of the electronic structures of BaSn$_3$, BaPb$_3$ (BaPb$_3$- and Mg$_3$In-type), SrSn$_3$ and SrPb$_3$. (r_{MT}: Muffin tin radius; K_{max}: maximal wavevector for the PW in the interstitium; BCP: bond critical point; RCP: ring critical point; IBZ: irreducible part of the *Brillouin* zone; V_{BB}: volume of the *Bader* basins).

Compound		BaSn$_3$	BaPb$_3$		SrSn$_3$	SrPb$_3$
Structure type		Ni$_3$Sn	BaPb$_3$	Mg$_3$In	Mg$_3$In	Cu$_3$Au
Crystal data		[5]	[11]	Tables 2 and 3	[3]	
R_{MT} (all atoms)		⊢		127.0 pm (2.4 a.u.)		⊣
$R_{MT} \cdot K_{max}$		⊢		8.0		⊣
k-points/BZ		820	1000	⊢　　1000	⊣	1295
k-points/IBZ		72	110	⊢　　110	⊣	75
Monkhorst-Pack-Grid		9 × 9 × 10	10 × 10 × 10	⊢　10 × 10 × 10	⊣	10 × 10 × 9
DOS		⊢		Figure 12		⊣
Band structure		[3,10,11]			[3]	[10,11]
Bonds:	label					
Electron	a	0.237 (305.9)	0.204 (319.3)	0.218 (315.0)	0.245 (302.6)	0.125 (351.4)
density	b	0.171 (326.7)	0.143 (343.7)	0.138 (346.4)	0.168 (339.2)	
at BCP/RCP(**r**)	c		0.138 (345.3)	0.136 (346.6)	0.147 (329.2)	
[$e^- 10^{-6}$ pm^{-3}]	d		0.109 (364.5)	0.133 (347.8)	0.159 (334.6)	
(d [pm])	e			0.131 (350.7)	0.150 (337.4)	
	f			0.093 (378.0)	0.116 (359.4)	
	r	0.190	0.152	0.164	0.198	0.088
Atoms:	label					
Charge	Sr/Ba(1)	+1.137 (28.6)	+1.093 (28.6)	+1.071 (28.5)	+1.255 (20.1)	+1.233 (20.3)
distribution	Sr/Ba(2)		+1.067 (28.4)	+1.069 (28.2)	+1.249 (19.8)	
after *Bader*	Sn/Pb(1)	−0.379 (32.1)	−0.359 (34.0)	−0.370 (33.9)	−0.440 (31.5)	−0.418 (34.5)
(V_{BB} [10^6 pm^3])	Sn/Pb(2)		−0.358 (34.5)	−0.344 (34.5)	−0.395 (31.6)	

3. Results and Discussion

3.1. Description of the Crystal Structures and Their Respective Phase Widths

The structures of all tri-tetrelides exhibit hexagonal close packed ordered AM_3 layers containing M kagomé (3.6.3.6.) nets. Depending on the stacking sequence, the M polyanion resembles the oxygen substructure of the hexagonal [face-sharing octahedra, |:AB:| ≡ h stacking, Ni$_3$Sn-type, border compound BaSn$_3$, Figure 1a] or the cubic [corner-sharing octahedra, |:ABC:| ≡ c stacking, Cu$_3$Au-type, border phase SrPb$_3$, Figure 1f] perovskite. In between these border phases, a series of structures occur, in which the amount of cubic stacking increases continuously and simultaneously the size of the blocks of face-sharing octahedra decreases.
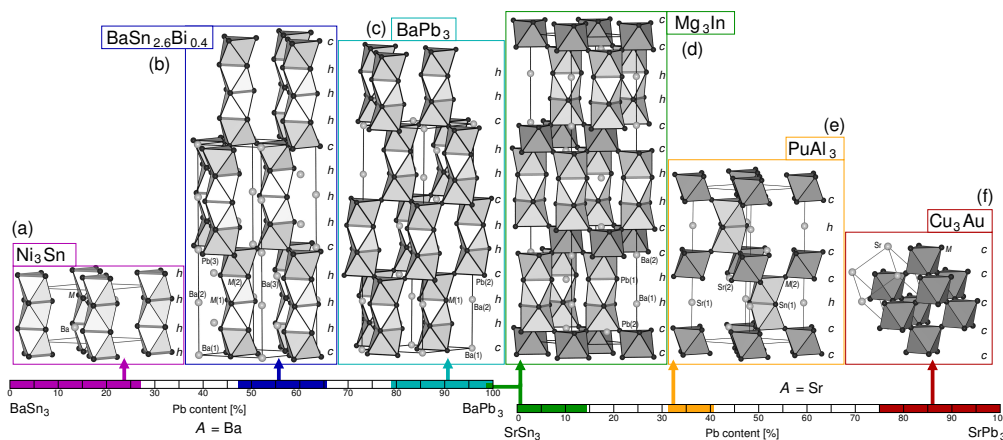

Figure 1. Crystal structures and phase widths (coloured bars) of the different stacking sequences observed in barium (left) and strontium (right) tri-stannides/plumbides (cf. the Figures 2–7 for enlarged views supplemented by the labeling of interatomic distances).

3.1.1. Ni$_3$Sn-Type Compounds

In the long-known binary stannide BaSn$_3$ [4,5], which forms the hexagonal Ni$_3$Sn-type (*hP8*, $P6_3/mmc$), up to 28% of the Sn atoms can be substituted against Pb (magenta bar in Figure 1). The crystal structure of the lead-richest phase BaSn$_{2.16}$Pb$_{0.84}$ (**1**) is depicted in Figure 2 in a polyhedra representation. The interatomic distances of this mixed stannide/plumbide are collected in Table 5. The pure *h* stacking of the hexagonal planar layers [BaM_3] results in infinite columns of [$M_{6/2}$] octahedra sharing two opposite faces, which are running along the *c* axis.
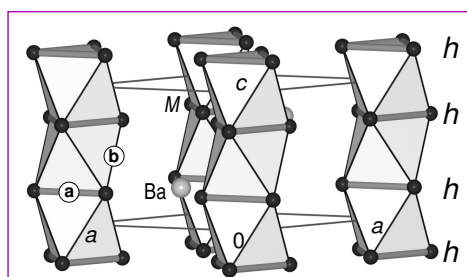

Figure 2. Crystal structure of BaSn$_{2.16}$Pb$_{0.84}$, **1** (Ni$_3$Sn-type; bond distances cf. Table 5 [35]).

Table 5. Selected interatomic distances (pm) in the crystal structure of BaSn$_{2.16}$Pb$_{0.84}$, **1** (Ni$_3$Sn-type). (cf. Figure 2 for the distance labels).

Atoms		Distance	freq.	CN		Atoms		Distance	lbl.	freq.	CN
Ba	$-M$	364.2(1)	6×		M		$-M$	313.6(2)	**a**	2×	
	$-M$	366.3(1)	6×	12			$-M$	332.0(1)	**b**	4×	
							$-$Ba	364.2(1)		2×	
							$-$Ba	366.3(1)		2×	10
							$-M$	412.6(2)		2×	+2

[M_3] three-membered rings with short M–M bonds of length 313.6 pm (label **a**) form the common faces of the [M_6] octahedra of the columns. The remaining octahedra edges are with 332.0 pm (**b**) significantly larger. In the planar M kagomé (3.6.3.6.) nets of the [BaM_3] hexagonal layers, the two remaining M–M contacts are strongly elongated and lie with a distance of 412.6 pm clearly outside any bonding range. Thus, the [M_3] triangles of the 3.6.3.6. net are alternatingly compressed and expanded. Therewith, the M coordination is reduced from the anticuboctahedral 12 (8 M and 4 Ba) surrounding in the ideal hexagonal close packing to an overall 10 (6 + 4) coordination. Compared to the binary border phase BaSn$_3$ [4], the M–M bond lengths (e.g., d_{Sn-Sn}^a = 305.3 pm) and the unit cell volume (cf. discussion in Section 3.3) are increased as expected. The barium cations are coordinated by 12 Sn/Pb atoms in a next to regular anticuboctahedral fashion, with Ba–M distances of 364.2 and 366.3 pm.

3.1.2. BaSn$_{2.6}$Bi$_{0.4}$-Type Compounds

An increased lead content of 47 to 66% (dark blue bar in Figure 1) causes the formation of the hexagonal BaSn$_{2.6}$Bi$_{0.4}$-type (*hP32*, $P6_3/mmc$, [18]) with a $(hhhc)_2$ stacking and blocks of four face-sharing octahedra (Figure 3). Selected interatomic distances of both border phases of this type, BaSn$_{1.58}$Pb$_{1.42}$ (**2**) and BaSn$_{1.01}$Pb$_{1.99}$ (**3**), are collected in Table 6.

The structure type contains both three crystallographically different barium and three M sites (Table 3). The latter are unequally taken by Sn and Pb: The M(3) position, which forms the [Ba(1) Pb(3)$_3$] layers of the *c* stacking is occupied by lead exclusively. Reversely, the M(1) position of a *h* stacked layer with pure *h* neighbor layers shows the lowest lead content (9.5–23.7%). The intermediate M(2) position of the hexagonal stacked [BaM(2)$_3$] layer with an adjacent *h* and *c* layer contains an intermediate amount of lead (40.1–70.6%). According to the stacking, the M(1) and M(2) atoms of

the *h* layers show a 6 + 4 coordination and form kagomé nets with two different triangles, whereas the lead atoms Pb(3) exhibit the ideal 8 + 4 surrounding and form an ideal 3.6.3.6. net among each other. The [*M*(1)$_3$] three-membered rings forming the common faces between face-sharing octahedra contain the shortest *M*–*M* bonds within the structure ($d^\mathbf{a}$ = 302.8–306.3 pm), whereas the analogous [*M*(2)$_3$] ring is enlarged due to the increased Pb proportion ($d^\mathbf{c}$ = 313.3–318.5 pm). All Ba cations are coordinated by 12 *M* atoms in a cuboctahedral [Ba(1) and Ba(3)] or anticuboctahedral [Ba(2)] manner. The Ba–*M* distances are all lying in the narrow range 363.4 to 369.4 pm.
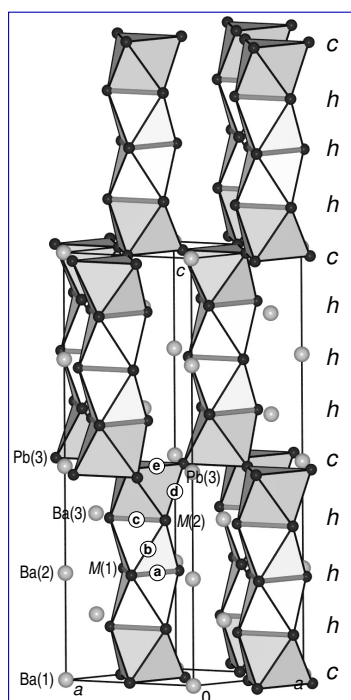
Figure 3. Crystal structure of BaSn$_{1.58}$Pb$_{1.42}$, **2** (BaSn$_{2.6}$Bi$_{0.4}$-type; bond distances cf. Table 6 [35]).

Table 6. Selected interatomic distances (pm) in the crystal structures of the two border compounds BaSn$_{1.58}$Pb$_{1.42}$ (**2**) and BaSn$_{1.01}$Pb$_{1.99}$ (**3**) of the BaSn$_{2.6}$Bi$_{0.4}$-type (cf. Figure 3 for the distance labels).

Atoms		Distances in		freq.	CN	Atoms		Distances in		lbl.	freq.	CN
		2	**3**					**2**	**3**			
Ba(1)	−Pb(3)	363.4(1)	364.1(1)	6×		*M*(1)	−*M*(1)	302.8(3)	306.3(2)	**a**	2×	
	−*M*(2)	366.6(1)	366.5(1)	6×	12		−*M*(2)	332.4(1)	336.2(1)	**b**	4×	
							−Ba(3)	354.5(2)	356.3(1)		2×	
							−Ba(2)	365.1(1)	365.6(1)		2×	6 + 4
Ba(2)	−*M*(1)	365.1(1)	365.6(2)	6×								
	−*M*(2)	368.5(1)	369.4(1)	6×	12	*M*(2)	−*M*(2)	313.3(2)	318.5(1)	**c**	2×	
							−*M*(1)	332.4(1)	336.2(1)	**b**	2×	
Ba(3)	−*M*(1)	354.5(2)	356.3(1)	3×			−Pb(3)	340.9(1)	343.1(1)	**d**	2×	
	−*M*(2)	365.4(1)	365.8(1)	6×			−Ba(3)	365.4(1)	365.8(1)		2×	
	−Pb(3)	368.2(2)	369.3(1)	3×	12		−Ba(1)	366.6(1)	366.5(1)			
							−Ba(2)	368.5(1)	369.4(1)			6 + 4
						Pb(3)	−*M*(2)	340.9(1)	343.1(1)	**d**	4×	
							−Pb(3)	363.4(1)	364.1(1)	**e**	4×	
							−Ba(1)	363.4(1)	364.1(1)		2×	
							−Ba(3)	368.2(2)	369.3(1)		2×	8 + 4

3.1.3. BaPb$_3$-Type Compounds

The stability range of the rhombohedral BaPb$_3$-type sequence $(hhc)_3$ ($hR36$, $R\bar{3}m$, Figure 4) starts at a lead proportion of 78% and reaches up to the pure plumbide BaPb$_3$ [9] (cyan bar in Figure 1). This structure type, which should be termed BaPb$_3$-type in consideration of the first structure determination in 1964 [9], is sometimes also denoted as TaCo$_3$-type. The interatomic distances of the Sn-richest border phase BaSn$_{0.65}$Pb$_{2.35}$ (**4**) are summarized in Table 7.
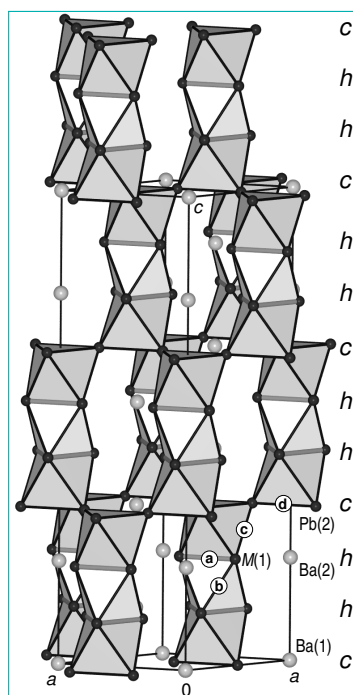
Figure 4. Crystal structure of BaSn$_{0.65}$Pb$_{2.35}$, **4** (BaPb$_3$-type; bond distances cf. Table 7 [35]).

Table 7. Selected interatomic distances (pm) in the crystal structure of BaSn$_{0.65}$Pb$_{2.35}$ (**4**) forming the BaPb$_3$-type (cf. Figure 4 for the distance labels).

Atoms		Distance	freq.	CN	Atoms		Distance	lbl.	freq.	CN
Ba(1)	$-M(1)$	360.0(2)	3×		$M(1)$	$-M(1)$	314.2(3)	a	2×	
	$-$Pb(2)	364.8(2)	3×			$-M(1)$	339.5(2)	b	2×	
	$-M(1)$	366.0(1)	6×	12		$-$Pb(2)	342.6(1)	c	2×	
						$-$Ba(1)	360.0(2)			
Ba(2)	$-$Pb(2)	364.4(1)	6×			$-$Ba(1)	366.0(1)		2×	
	$-M(1)$	368.3(1)	6×	12		$-$Ba(2)	368.3(1)			6 + 4
					Pb(2)	$-M(1)$	342.6(1)	c	4×	
						$-$Pb(2)	364.4(1)	d	4×	
						$-$Ba(2)	364.4(1)		2×	
						$-$Ba(1)	364.8(2)		2×	8 + 4

In the lead-rich compounds of the Ba series, the planar nets [BaM_3] follow the rhombohedral $(hhc)_3$ stacking sequence and the blocks of face-sharing octahedra are now consisting of three octahedra only (Figure 4). Within these trimers, the [M_6] octahedra share common triangular faces [$M(1)_3$] with the shortest interatomic distances of the whole structure ($d^{\mathbf{a}}$ = 314.2 pm, cf. Table 7). As expected from the tin content, this and all further M–M distances are somewhat shortened with respect to the isotypic pure plumbide (e.g., $d^{\mathbf{a}}$ = 319.3 pm, [11]). The octahedra trimers are connected via the six corners formed by the pure lead position [Pb(2)]. According to the point group symmetry $.\frac{2}{m}$ of the

Pb(2) position, these atoms form ideal kagomé nets at $z = 0$, $\frac{1}{3}$ and $\frac{2}{3}$ in the unit cell. The mesh width of this net, i.e., the Pb(2)–Pb(2) distances (4×) are comparatively large 364.4 pm, whereas the remaining M–M distances are of intermediate lengths (339.5 and 342.6 pm). Again, the atoms forming the h layers exhibit a 6 + 4 coordination, whereas the c net position [Pb(2)] has the full 8 M + 4 Ba surrounding of a dense packing. The Ba(1) cations show a cuboctahedral, Ba(2) an anticuboctahedral, both fairly regular ($d_{Ba-M} = 360.0$–368.3 pm), twelvefold M coordination.

3.1.4. Mg$_3$In-Type Compounds

A second new polymorph of BaPb$_3$ (denoted BaPb$_3$-II hereafter) crystallizes in the Mg$_3$In-type structure with a further increased amount of cubic sequences [$(hhcc)_3$; $hR48$, Figure 5]. This form of BaPb$_3$ is thus isotypic with the border phase SrSn$_3$ [3] of the respective Sr series and with the lead-containing compounds up to a Pb content of 14% (SrSn$_{2.58}$Pb$_{0.42}$, **5p**; green bar in Figure 1). The structure model of these compounds should be denoted Mg$_3$In-type, because the crystallographic data of this particular compound were the first one published in 1963 [28]. Two years later, an isotypic structure was reported for the high-temperature form of PuGa$_3$ and only much later (2000, [3]) the tri-stannide SrSn$_3$ was added. The two latter compounds are nevertheless widely (e.g., in the *Inorganic Crystal Structure Database* [39]) used to address this structure type.
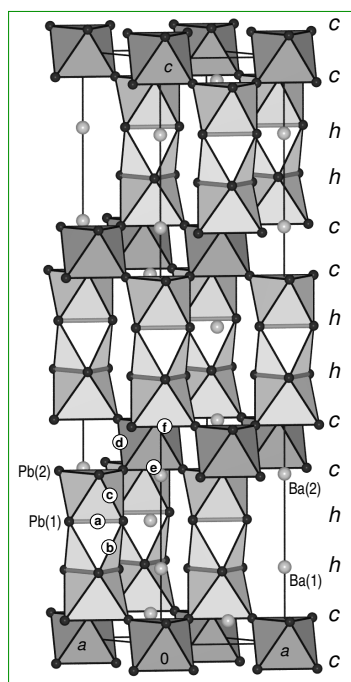
Figure 5. Crystal structure of BaPb$_3$-II, **5** (Mg$_3$In-type; bond distances cf. Table 8 [35]).

In the structure of BaPb$_3$-II (Figure 5) the rhombohedral stacking sequence $(hhcc)_3$ results in octahedra trimers, which are not directly connected via corners as in BaPb$_3$-I, but an additional layer of corner-connected [Pb(2)$_6$] octahedra is interspersed. Overall, a 1:1 relation of h and c layers, i.e., Pb(1) and Pb(2) atoms, are reached. In addition, in this case, the Pb–Pb distances of the common [Pb(1)$_3$] triangles of the face-sharing lead octahedra are with 315.0 pm the shortest bonds within the structure. All other Pb–Pb distances are found in the range 346–378 pm, whereby the largest values are again in the c-stacked kagomé nets [Pb(2)–Pb(2)]. In contrast to the c layers in the BaPb$_3$-type structures, the 3.6.3.6. Pb(2) nets exhibit two different triangles with Pb(2)–Pb(2) edges of 350.7 and 378.0 pm. Nevertheless, the [Pb(2)$_3$] triangles in the h layers are much more different in size (315.0/413.7 pm). Due to these compressed/expanded triangles, the Pb(1) atoms of the common octahedra faces are surrounded by 6 Pb and 4 Ba cations only, whereas Pb(2) of the c net exhibits the complete 12-fold coordination, even

though two lead neighbors are already at a slightly larger distance than the four Ba cations (Table 8). The cations themselves again show the ideal 12-fold lead coordination, with 50% cuboctahedral [Ba(2)] and 50% anticuboctahedral [Ba(1)] arrangement. The Mg_3In-type structure has been already observed (and predicted by *van Vucht* in 1966 [7]) for pure plumbides with a small substitution of barium by calcium or strontium (for $A_xBa_{1-x}Pb_3$: $x = 0.03$ for Ca and 0.10 for Sr [11]). It also occurs in the compound series $Ba(Sn_xBi_{1-x})_3$ [18] and from $SrSn_3$ to $SrSn_{2.58}Pb_{0.42}$ (**5p**). Unfortunately (due to problems with the crystal quality in the Sr series, cf. Section 2.2) the structure of the latter compound has been refined from powder data only (Section 2.3). As expected, the lattice parameters and all *M*–*M* bonds are slightly elongated compared to $SrSn_3$ and the lead atoms are substituted at the *c* stacked layers, i.e., the *M*(2) position.

Table 8. Selected interatomic distances (pm) in the crystal structure of $BaPb_3$ (Mg_3In-type structure). (cf. Figure 5 for the distance labels).

Atoms		Distance	freq.	CN	Atoms		Distance	lbl.	freq.	CN
Ba(1)	–Pb(1)	361.7(2)	3×		Pb(1)	–Pb(1)	315.0(2)	a	2×	
	–Pb(2)	365.6(2)	3×			–Pb(1)	346.4(2)	b	2×	
	–Pb(1)	366.2(1)	6×	12		–Pb(2)	346.6(1)	c	2×	
						–Ba(2)	361.6(2)			
Ba(2)	–Pb(1)	361.6(2)	3×			–Ba(1)	361.7(2)			
	–Pb(2)	364.6(1)	6×			–Ba(1)	366.2(1)		2×	6 + 4
	–Pb(2)	365.0(2)	3×	12						
					Pb(2)	–Pb(1)	346.6(1)	c	2×	
						–Pb(2)	347.8(2)	d	2×	
						–Pb(2)	350.7(2)	e	2×	
						–Ba(2)	364.6(1)		2×	
						–Ba(2)	365.0(2)			
						–Ba(1)	365.6(2)			
						–Pb(2)	378.0(2)	f	2×	6 + 4 + 2

In the vast series of tri-metallides of the structure family considered, polymorphism (like the one observed herein for $BaPb_3$) is very frequent. An instructive example are the tri-gallides of the rare earth elements, were the smaller Er, Tm and Lu cations form Cu_3Au-type structures, whereas Tb, Dy and Ho are di- or even trimorphic [40]. For the two modifications of $BaPb_3$, the difference of the unit cell volumes per formula unit (*V*/f.u.) is even smaller than 0.1% [131.16 (I) compared to 131.07×10^6 pm^3 (II)] and an experimental hint towards the phase relation between the two polymorphs is also not obvious.

3.1.5. $PuAl_3$-Type Compounds

In the Sr series, a Pb content of 32% ($SrSn_{2.05}Pb_{0.95}$, **6**) to 41% ($SrSn_{1.77}Pb_{1.23}$, **6p**) causes a small existence region of the hexagonal $PuAl_3$-type ($hP24$, $P6_3/mmc$ [41]) with a $(hcc)_2$ stacking (golden bar in Figure 1). The structure and selected bond lengths are found in Figure 6 and Table 9.

The increased proportion of *c* stacking in the $PuAl_3$-type reduces the size of the blocks of face-sharing octahedra to dimers, which are separated by additional *c* stacked [*M*(2)6] corner-sharing octahedra. Again, tin prefer the occupation of the *h* layer and the shortest distances are found in the common face triangle inside this layer ($d^{\mathbf{a}}_{Sn(1)–Sn(1)} = 302.9$ pm). The triangles of the *h* net are thus of very different size, whereas the *M*(2) kagomé nets of the *c* layers are only slightly distorted (345.0, **d**/352.0, **e** pm). The overall coordination of the *h* and *c* layer *M* atoms and the strontium cations again fits the situation throughout the whole structure family.
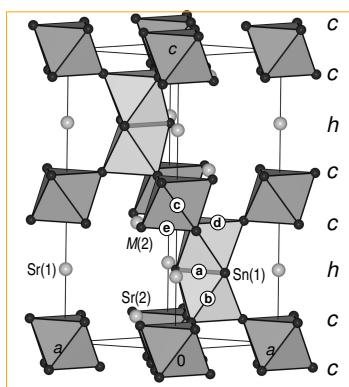
Figure 6. Crystal structure of $SrSn_{2.05}Pb_{0.95}$, **6** (PuAl$_3$-type; bond distances cf. Table 9 [35]).

Table 9. Selected interatomic distances (pm) in the crystal structure of $SrSn_{2.05}Pb_{0.95}$ (PuAl$_3$-type). (cf. Figure 6 for the distance labels).

Atoms		Distance	freq.	CN	Atoms		Distance	lbl.	freq.	CN
Sr(1)	$-M(2)$	348.4(2)	6×		Sn(1)	$-Sn(1)$	302.9(8)	a	2×	
	$-Sn(1)$	349.5(1)	6×	12		$-M(2)$	339.9(2)	b	4×	
						$-Sr(2)$	347.8(6)		2×	
Sr(2)	$-Sn(1)$	347.8(6)	3×			$-Sr(1)$	349.5(1)		2×	6 + 4
	$-M(2)$	349.1(1)	6×			$-Sn(1)$	394.1(8)		2×	
	$-M(2)$	353.2(7)	3×	12						
					$M(2)$	$-M(2)$	339.3(4)	c	2×	
						$-Sn(1)$	339.9(2)	b	2×	
						$-M(2)$	345.0(4)	d	2×	
						$-Sr(1)$	348.4(2)			
						$-Sr(2)$	349.1(1)		2×	
						$-M(2)$	352.0(4)	e	2×	
						$-Sr(2)$	353.2(7)			8 + 4

3.1.6. Cu$_3$Au-Type Compounds

The strontium series is terminated by the pure $(c)_3$ stacking of SrPb$_3$ (Cu$_3$Au-type, $cP4$, $Pm\bar{3}m$), which starts at a lead content of approximately 75%. Because of problems with the single crystal quality, a reliable refinement of the Sn/Pb occupation was not possible, so that some uncertainty of the exact composition remains. The very broad reflections of the powder diffraction pattern prohibit even a full-pattern *Rietveld* refinement and a decision is not possible, whether the tetragonal distortion of the cubic Cu$_3$Au-type, which is reported in the literature for the binary tri-plumbide SrPb$_3$ [6], also arises in the ternary tin-containing phase.
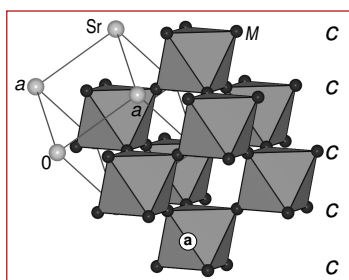
Figure 7. Crystal structure of $SrSn_{0.75}Pb_{2.25}$, **7** (Cu$_3$Au-type; bond distances cf. Table 10 [35]).

In accordance with the presence of smaller Sn atoms, the lattice parameter and therewith the M–M distance of 350.3 pm is somewhat decreased compared to the two distances found in the tetragonal

border phase $SrPb_3$ (d_{Pb-Pb} = 351.1, 353.2 pm [6]). The structure terminates the series with a pure *c* stacking and a polyanion, which consists of ideal corner-sharing $[M_{6/2}]$ octahedra. All atoms exhibit an ideal cuboctahedral surrounding with one unique distance of 350.3 pm (cf. Table 10).

Table 10. Selected interatomic distances (pm) in the crystal structure of $SrSn_{0.75}Pb_{2.25}$ (Cu_3Au-type structure).

Atoms		Distance	freq.	CN	Atoms		Distance	lbl.	freq.	CN
Sr	−*M*	350.3(1)	12×	12	*M*	−*M*	350.3(1)	a	6×	
						−Sr	350.3(1)		6×	6 + 6

3.2. Stacking Sequences: Geometric Aspects

The series of mixed Sn/Pb tri-tetrelides discussed above, as well as similar systematic studies on mixed Ca/Sr/Ba stannides [10] and plumbides [11], clearly show, that the amount of *h/c* stacking in the structure family of AB_3 superstructures of dense sphere packing and hence the sequence of the different structure types is essentially determined by the radius ratio of the two elements. This becomes apparent from the coherent progress of the amount of hexagonal stacking with the radius ratio of the two elements shown in Figure 8. Similar plots are presented for a great variety of compounds in the literature [7,8]. In contrast to these works, in which metallic radii were used to estimate the atomic sizes, ionic radii (after *Shannon* [42], for CN = 12) were used herein to estimate the size of the *A* cations, and metallic radii (after *Gschneidner* [43], for CN = 12) were only applied to quantify the size of the Sn and Pb atoms. This choice of radii is in agreement with the next to complete electron transfer from the alkaline-earth elements *A* to Sn/Pb (cf. Section 3.5.2). The diagram shown in Figure 8 demonstrates the direct relation between the stacking sequence and the radius ratio, independent of the type of the *M* atom, i.e., both for Sn (squares and thin dashed line), Pb (circles and thin solid line) or Sn and Pb (with a distinct distribution at the *h/c* layer, colored triangles and bold lines).
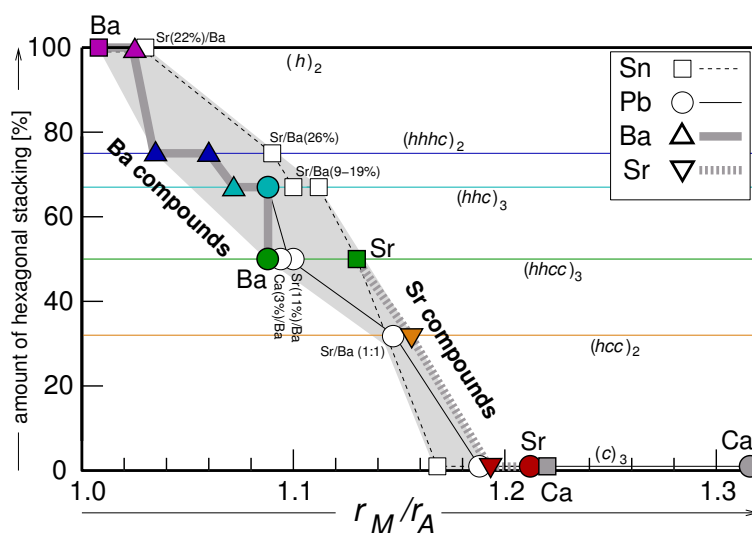
Figure 8. Amount of hexagonal stacking plotted versus the radius ratio r_M:r_A in (mixed) alkaline-earth tri-stannides (thin squares and dashed line) and -plumbides (thin circles and line) and the mixed stannides/plumbides (triangles and bold gray lines) reported in this work.

This general behaviour can be explained by the decreased (10) coordination number of the atoms of the *h* layers (6 × *M* + 4 × *A*) compared to the ideal twelvefold (8×*M* + 4×*A*) coordination of the *M* atoms of *c* stacked layers (Figure 9).

However, the reason for the reduction of the coordination sphere of *h*-type atoms from 12 to 10 is the compression of the common $[M_3]$ triangle of two face-sharing octahedra, which is causally linked to covalent bonding contributions within the *M* polyanion (cf. Section 3.5).
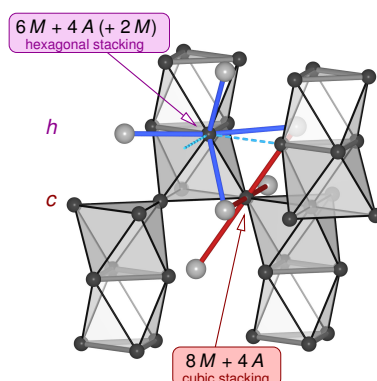

Figure 9. Comparison of the characteristic coordination spheres of Sn/Pb atoms of a hexagonal (violet-blue) and a cubic (red) stacked layer [35].

In electron poorer compounds (like for example $CaHg_3$ or $SrHg_3$ [44]), which crystallize in the Ni_3Sn-type, the *M–M* triangles do not show shortened edges/bonds (cf. also the discussion on the value of the atomic *x* parameter in the Ni_3Sn and related structures by *Havinga* in [8]).

3.3. Molar Volumes and Variation of the c/a Ratio

Regardless of the different stacking sequences, the molar volumes of all tri-tetrelides follow *Vegards* rule (gray circles and thin black lines in Figure 10). The normalized interlayer distance, i.e., the *c/a* ratio/two layers (open circles and gray lines) decreases continuously with (i) increasing *h* stacking (thick gray lines) and (ii) with the Sn content of each distinct structure type. This increasing hexagonal unit cell basis is a consequence of the covalent bonding contributions and the stereochemically active lone electron pair (l.e.p., see Section 3.5) of the tin (and less pronounced the lead) atoms of the *h* layers in the electron-richer compounds of the AB_3 structure family. Simple packing/geometric arguments failed to explain this general trend, which is similarly observed for other electron-richer compounds of this structure family [7,8].
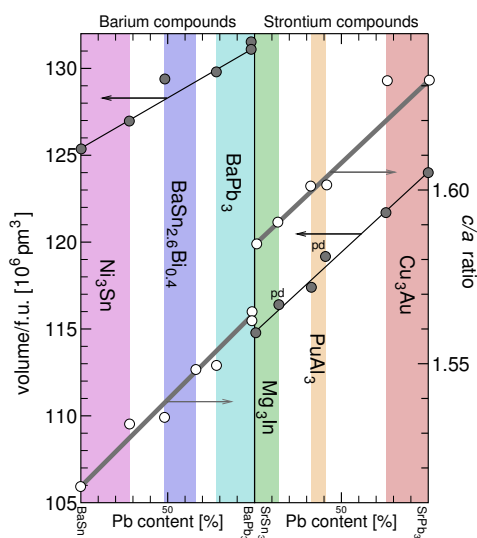
Figure 10. Normalized unit cell volumes *V*/f.u. and *c/a* ratios (for two layers) of the mixed tri-stannides/plumbides of barium (left) and strontium (right).

3.4. Sn/Pb Distribution: 'Coloring' Aspects

Concerning the 'coloring' [19], i.e., the preference of tin and lead to occupy the differently stacked layers, the clear preference of Sn atoms to occupy the *h* nets is valid throughout the whole family of the tri-tetrelides. Arguments for this very uniform coloring are at one hand the reduced coordination sphere of the *h* layer atoms (cf. Section 3.2), which may better fit the smaller *M* atom types. On the other hand, the larger Sn–Sn (compared to Pb–Pb) single bond energies direct tin to take those sites in the structure, where generally the shortest bonds are formed; this is unequivocally the *h* position.

3.5. Chemical Bonding, Electronic Structure

Calculations of the electronic band structure, based on different levels of theory, are already reported in vast detail for several border phases of the title compound series. The results of LMTO-ASA calculations of $SrSn_3$ [3] and $BaSn_3$ [5] are in very good agreement with the FP-LAPW results discussed in [10,11]. The obtained electron densities of these DFT calculations reveal the different types of Sn–Sn bonds as well as the presence of the l.e.p. at the *h*-stacked tin atoms [10]. The related ELF exhibits comparatively low (approx. 0.6) maxima at the bonds of the common octahedra edges and for the l.e.p. of *h*-type atoms [3]; whereas the ELF obtained from EH calculations shows significantly more pronounced features (e.g., [5] for $BaSn_3$). The band structures of the cubic phases like $CaPb_3$ and $SrPb_3$ were also calculated using FP-LMTO [14] and FP-LAPW [10,11] methods. A detailed discussion of the band structure from the point of view of chemical bonding can be found in [10]. In this work, the literature's theoretical work is complemented by FP-LAPW calculations of the new polymorph of $BaPb_3$, which—according to its isotypy to $SrSn_3$—allows for a direct comparison of an Sn with an isotypic (Mg_3In-type) Pb compound. Corresponding calculations of the border phases $BaSn_3$, $BaPb_3$-I, $SrSn_3$ and $BaPb_3$ (Table 4) are also included for comparison and for a detailed analysis of the electron density. Independent of the stacking of the close-packed layers, the total density of states (tDOS) show pronounced minima next to the *Fermi* level (14 v.e./f.u.), which implies the validity of simple electron counting rules.

3.5.1. Electron Count (*Zintl/Wade/mno*)

Compounds with the pure *h* stacking like e.g., $BaSn_3$ exhibit three-membered rings with short *M*–*M* bonds, which are only slightly larger than single bond distances, and the calculated electron density shows the highest electron density at the respective bond critical points ($\rho_{BCP} = 0.237\,e^{-}10^{-6}\,pm^{-3}$, Table 4 and [10]). Neglecting all further *M*–*M* contacts—as proposed in [5]—the compound contains *Zintl* anions $[M_3]^{2-}$ with an aromatic π system of two electrons. Admittedly, the results of the band structure calculations [10] show, that this simplified model is only of limited applicability: No (pseudo) band gap can be found at the *Fermi* level (cf. Figure 12) and the number of p_z-type bands below E_F is not compatible with an aromatic π system. However, the evident stability of the whole structure family at (or close to) 14 v.e. per formula unit (i.e., $4\frac{2}{3}$ v.e./*M*) can be explained both for the *h* and the *c* stacking (and therewith also for all stacking variants in between) when taking the 'polyaromatic' bonding character (cf. the longer *M*–*M* bonds and the ring critical points, Section 3.5.2) into account and extending the *Zintl* concept by *Wade*'s electron counting rules [45] or the somewhat more comprehensive *mno* rule of *Jemmis* [46]:

c The bonding within *c* stacked compounds like e.g., $SrPb_3$, in which $[Pb_6]$ octahedra are fused via common corners (Figure 7), can be explained by a direct comparison with the electron-precise boride CaB_6 containing also octahedral *closo* clusters B_6^{2-} (20 v.e.), which are in this case connected via 2e2c bonds (*exo*-bonds). Subtracting the six v.e. needed for these *exo*-bonds, each boron atom contributes $2\frac{1}{3}$ v.e. to stabilize one octahedral *closo* cluster. In tri-tetrelides two octahedra are directly fused via corners, i.e., each Pb atom participates in two *closo* octahedral clusters. Thus, the polyanion needs $2 \times 2\frac{1}{3} = 4\frac{2}{3}$ v.e./Pb to obey *Wade*'s rule. This corresponds to the observed v.e. number ($2SrPb_3 \longrightarrow 2Sr^{2+} + Pb_6^{4-}$: $6{\times}4 + 4$ v.e./f.u. $\equiv 4\frac{2}{3}$ v.e./Pb). and to the fact, that the

tDOS exhibits a very pronounced minimum close to the *Fermi* level, at 13.9 v.e./f.u. (bottom of Figure 12, black arrow).

h   The *mno* rules and the similarities to the 'polyaromatic' bonding in borides and molecular boranes/boranates can be also used to explain the electron count of the *h* stacked atoms: Figure 11 shows the formal splitting of the v.e. in the boranate $[B_9H_6]^-$, which satisfies the *mno* rules [46] $(9 + 2 + 0 = 11$ s.e.p. (s.e.p.: skeleton electron pairs): $\underbrace{9 \times 3}_{B} + \underbrace{6 \times 1}_{H} + \underbrace{1}_{charge} - \underbrace{6 \times 2}_{exo\text{-}BH} = 22$ s.e. $= 11$ s.e.p.). For the formal splitting of these overall number of s.e. to individual B atoms, the six BH atoms contribute 14 s.e. $(6 \times 2\frac{1}{3}$, see above). The remaining 8 s.e. result in $2\frac{2}{3}$ v.e. for each of the three central (*h* stacked) B atoms ($1\frac{1}{3}$ s.e./octahedron). Transfered to the electron balance of $BaSn_3$, where each of the Sn atoms carries an additional lone-electron pair (s^2 electrons), we expect $2 + 2\frac{2}{3} = 4\frac{2}{3}$ v.e./Sn (i.e., 14 v.e./f.u.) to result in a stable cluster.
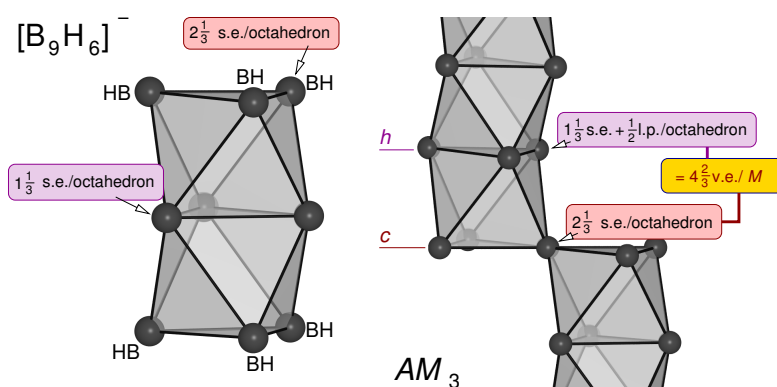
Figure 11. Explanation of the electron count proving the validity of the *Wade-Jemmis mno* rules for the hexagonal and cubic stacking in alkaline-earth tri-tetrelides.

The uniform ideal v.e. number for both the *h* and *c* stacked *M* atoms of $4\frac{2}{3}$ v.e./*M* explains the stability of the polyanion in all tri-tetrelides AM_3, i.e., for compounds with 14 v.e./f.u.

3.5.2. Bandstructure Calculations (DOS, Electron Densities)

In accordance with the electron count discussed above, the calculated total densities of states (tDOS) of all tri-tetrelides (cf. Figure 12 and [10,11]) exhibit distinct minima close to 14 v.e., slightly below the *Fermi* level. The *M* pDOS of *c* and *h* layers are plotted in the familiar color code, magenta arrows indicate the position of the lone-electron pairs (l.e.p.) of the *s*-states of *h*-stacked *M* atoms. The pDOS of the *M* atoms of the polyanion are separated into overall non-bonding *M-s* ($-10...-4$ eV, 6 v.e./f.u.) and bonding *M-p* states (>-4 eV, 8 v.e./f.u.). As expected, this separation increases from the stannides to the plumbides. The low Sr/Ba pDOS below E_F (black lines in Figure 12) is in accordance with the positive *Bader* charges (q) of the *A* cations and the pronounced electron transfer from the alkaline-earth element towards the *p* block element. The cation charges vary slightly between $+1.07$ ($BaPb_3$) and $+1.26$ ($SrSn_3$) (Table 4). In mixed *h/c* stacked compounds, the different *M* atoms are comparably negatively charged, which is in agreement with the equal formal electron demand and the great importance of geometric parameters for the stacking sequences and the polyanion 'coloring'. Overall, the *M* charges vary between -0.34 and -0.42.
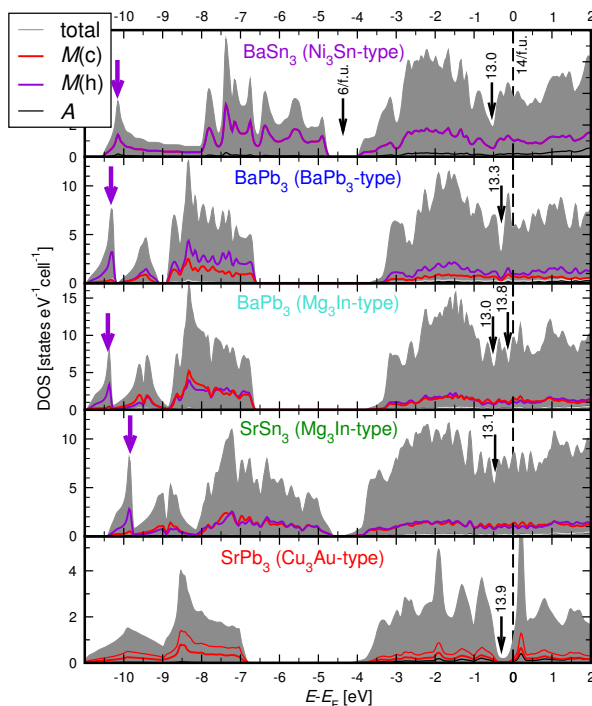
Figure 12. Density of states of the calculated alkaline-earth tri-tetrelides (in eV relative to the *Fermi* level; magenta/red: partial DOS of *M* atoms of a *h/c* layer).

The calculated electron density maps (cf. Figure 13 for a cross-section of the *h* layer in BaPb$_3$-II) exhibit bond (BCP) and ring (RCP) critical points of significant height $\rho_{\text{BCP/RCP}}$ ($>$0.1 e$^-$10^{-6} pm^{-3}) for all labelled *M*–*M* bonds. (In the tetrahedra/octahedra interstices ρ drops down to 0.02 e$^-$10^{-6} pm^{-3}). Thereby ρ_{BCP} decrease with increasing *M*–*M* distances (Table 4). The largest values (i.e., strongest bonds) are found for the edges of the face-sharing [*M$_6$*] octahedra (label **a** in Figure 13). In the calculated ELF of both the stannides and the plumbides, only this bond (and the l.e.p.) is recognizable by a small maximum of approx. 0.6 (see also [4]). These three-membered rings are centered by distinct ring critical points of heights between 0.15 (Pb compounds, cf. Figure 13) and 0.20 e$^-$10^{-6} pm^{-3} (Sn compounds).
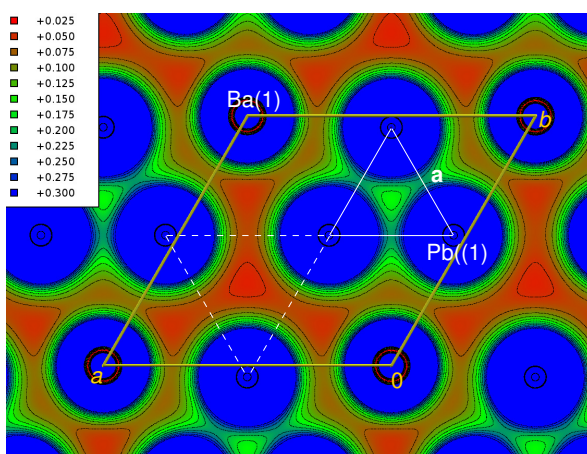
Figure 13. Cross-section of the calculated electron density map [e$^-$10^{-6} pm^{-3}] of the *h* section of BaPb$_3$-II.

The remaining faces of all $[M_6]$ octahedra depicted in the structure drawings above are also centered by RCP with somewhat smaller values of ρ_{RCP}. This and the analysis of the bandstructures of the border compounds $BaSn_3$, $CaPb_3$ and $BaPb_3$ themselves given in the literature [6,10,11,14,15] justify the description of the covalent bonding contributions in the tri-tetrelides as 'polyaromatic', i.e., as analogs of e.g., boron compounds. The $M–M$ distances, which are considerably increased compared to the single bond lengths, are also similar to the larger contacts observed e.g., in the electron-precise *nido* clusters M_9^{4-} of several alkali stannides/plumbides [47–52].

Nevertheless, polar compounds of this structure family are known to be electronically somewhat flexible and the minimum of the tDOS generally does not exactly coincide with the *Fermi* level. The comparison of the tDOS of tri-tetrelides with varying h/c stacking ratio displays tendencies towards a small decrease of the tDOS minimum with increasing h-stacked layers (cf. black arrows in Figure 12). A similar trend is obvious in the tin series $CaSn_3/SrSn_3/BaSn_3$, where the tDOS minima are found at 13.9/13.3/13 v.e./f.u. [10]. This shift is in accordance with several experimental observations [7,12,15], e.g., for Tl-substituted plumbides [16] and the series $BaBi_3–BaSn_3$ [18]: in both cases, the amount of h stacked layers increases continuously with decreasing v.e. numbers.

4. Summary

The reported systematic experimental, crystallographic and bond-theoretical DFT study of the series of mixed Sn/Pb (M) tri-tetrelides of Sr and Ba (A) AM_3 allows the study of the geometric and electronic criteria, which determine the stacking sequences of planar AM_3 hexagonal layers in the large family of close-packed AB_3 structures. The series of new compounds starts at the binary tri-stannide $BaSn_3$ with a pure hexagonal h_2 stacking ($NiSn_3$-type), in which up to 28% of the Sn atoms can be substituted against Pb. A further increased lead content of 47 to 66% causes the formation of the $BaSn_{2.6}Bi_{0.4}$-type structure with a $(hhhc)_2$ stacking. The stability range of the $BaPb_3$-type sequence $(hhc)_3$ starts at a lead proportion of 78% and reaches up to the pure plumbide $BaPb_3$. A second new polymorph of $BaPb_3$ forms the Mg_3In-type structure with a further increased amount of cubic sequences $[(hhcc)_3]$ and is thus isotypic with the border phase $SrSn_3$ of the respective Sr series. In this series, a Pb content of 32 to 41% creates an existence region of the $PuAl_3$-type with a $(hcc)_2$ stacking. The series is terminated by the pure c stacking of $SrPb_3$ (Cu_3Au-type), which starts at 75% Pb. Even though all compounds are metals, the calculated DOS exhibits pronounced pseudo band gaps slightly below E_F of 14 v.e./f.u. The minimum occurs independent of the type of stacking, so that geometric parameters (radius ratio of the atoms/cations) are the main parameters determining the layer sequence. The application of simple covalent bonding concepts (*Zintl* concept and *Wade/Jemmis mno* rules), which is justified by the distinct bond and ring critical points of the electron density maps, the features of the ELFs and the band structures themselves, allows for the explanation of these DOS minima at approx. 14 v.e./f.u. Nevertheless, metallic (i.e., steep bands crossing E_F) besides the covalent (flat bands near E_F) features are the main characteristic of the band structures of the tri-tetrelides and determine their specific physical properties like e.g., their superconductivity.

Author Contributions: Compound synthesis: M.L. and M.J.; Data collection (powder and single crystal): M.L. and M.J.; Structure refinements: M.L., M.J. and C.R.; Theoretical calculations: M.L., M.J. and C.R.; Writing: M.L., M.J. and C.R.

References and Notes

1. Fässler, T.F.; Hoffmann, S. Valence compounds at the border to intermetallics: alkali and alkaline earth metal stannides and plumbides. *Z. Kristallogr.* **1999**, *214*, 722–734. [CrossRef]
2. Hume-Rothery, W. Formation of intermetallic compounds. Part IV: The System Calcium-Tin and the compounds $CaSn_3$, $CaSn$ and Ca_2Sn. *J. Inst. Met.* **1926**, *35*, 319–335.

3. Fässler, T.F.; Hoffmann, S. SrSn₃–eine supraleitende Legierung mit freien Elektronenpaaren. *Z. Anorg. Allg. Chem.* **2000**, *626*, 106–112. [CrossRef]

4. Ray, K.W.; Thompson, R.G. Study of barium-tin alloys. *Met. Alloys* **1930**, *1*, 314–316.

5. Fässler, T.F.; Kronseder, C. BaSn₃, ein Supraleiter im Grenzbereich zwischen Zintl-Phasen und intermetallischen Verbindungen: Realraumanalyse von Bandstrukturen. *Angew. Chem.* **1997**, *109*, 2800–2803. [CrossRef]

6. Damsma, W.; Havinga, E.E. Influence of small lattice deformation on the superconductive critical temperature of alloys with the Cu₃Au type structure. *J. Phys. Chem. Solids* **1972**, *34*, 813–816. [CrossRef]

7. Van Vucht, J.H.N. Influence of radius ratio on the structure of intermetallic compounds of the AB₃ type. *J. Less Common Met.* **1966**, *11*, 308–322. [CrossRef]

8. Havinga, E.E. Influence of repulsive energy on structural parameters of the close-packed metal structures. *J. Less Common Met.* **1975**, *41*, 241–254. [CrossRef]

9. Sands, D.E.; Wood, D.H.; Ramsey, W.J. The structures of Ba₅Pb₃ , BaPb and BaPb₃. *Acta Crystallogr.* **1964**, *17*, 986–989. [CrossRef]

10. Wendorff, M.; Röhr, C. Gemischte Tristannide der Reihe CaSn₃–SrSn₃–BaSn₃: Synthesen, Kristallstrukturen, Chemische Bindung. *Z. Anorg. Allg. Chem.* **2011**, *637*, 1013–1023. [CrossRef]

11. Wendorff, M.; Röhr, C. Gemischte Plumbide (Ca/Sr)ₓBa₁₋ₓPb₃. Strukturchemie und chemische Bindung. *Z. Naturforsch.* **2008**, *63b*, 1383–1394.

12. Havinga, E.E. W-like dependence of critical temperature on number of valence electrons in non-transition metal Cu₃Au-type alloys. *Phys. Lett. A* **1968**, *28*, 350–351. [CrossRef]

13. Havinga, E.E.; Damsma, W.; van Maaren, M.H. Oscillatory dependence of superconductive critical temperature on number of valency electrons in Cu₃Au type alloys. *J. Phys. Chem. Solids* **1970**, *31*, 2653–2662. [CrossRef]

14. Baranovskiy, A.E.; Grechnev, G.E.; Svechkarev, I.V. Features of the electronic spectrum and anomalous magnetism in the compounds YbPb₃, YbSn₃, CaPb₃ and CaSn₃. *Low Temp. Phys.* **2006**, *32*, 849–856. [CrossRef]

15. Baranovskiy, A.E.; Grechnev, G.E.; Mikitik, G.P.; Svechakarev, I.V. Anomalous diamagnetism in the intermetallic compounds CaPb₃ and YbPb₃. *Low Temp. Phys.* **2003**, *29*, 356–358. [CrossRef]

16. Havinga, E.E.; van Vucht, J.H.N. The crystal structure of Ba(Pb₀.₈Tl₀.₂)₃. *Acta Crystallogr.* **1970**, *B26*, 653–655. [CrossRef]

17. Single crystal structure refinement of the strucuture of BaIn₀.₁₅Pb₂.₈₅: Hexagonal, space group *P*6₃/*mmc*, *a* = 733(1), *c* = 3991(5) pm, *Z* = 14, *R*1 = 0.0494.

18. Ponou, S.; Fässler, T.F.; Kienle, L. Structural complexity in intermetallic alloys: Long-periodic order beyound 10 nm in the system BaSn₃/BaBi₃. *Angew. Chem.* **2008**, *47*, 3999–4004. [CrossRef] [PubMed]

19. Miller, G.J. The "Coloring Problem" in solids: How it affects structure, composition and properties. *Eur. J. Inorg. Chem.* **1998**, *5*, 523–536. [CrossRef]

20. Yvon, K.; Jeitschko, W.; Parthé, E. *Program LAZY-PULVERIX*; University Geneve: Geneva, Switzerland, 1976.

21. STOE & Cie GmbH. *X-SHAPE (Version 1.03), Crystal Optimization for Numerical Absorption Correction*; STOE & Cie GmbH: Darmstadt, Germany, 2005.

22. Sheldrick, G.M. *SADABS: Program for Absorption Correction for Data from Area Detector Frames*; Bruker Analytical X-ray Systems, Inc.: Madison, WI, USA, 2008.

23. Sheldrick, G.M. A short history of SHELX. *Acta Crystallogr.* **2008**, *A64*, 112–122. [CrossRef] [PubMed]

24. Gelato, L.M.; Parthé, E. STRUCTURE TIDY: A computer program to standardize structure data. *J. Appl. Crystallogr.* **1990**, *A46*, 467–473. [CrossRef]

25. Further details on the crystal structure investigation are available from the Fachinformationszentrum Karlsruhe, Gesellschaft für wissenschaftlich-technische Information mbH, D-76344 Eggenstein-Leopoldshafen 2 on quoting the depository numbers CSD 431093 (BaPb₃-II), 431094 (BaSn₀.₆₅Pb₂.₃₅) 431095 (BaSn₁.₀₁Pb₁.₉₉) 431096 (BaSn₁.₅₂Pb₁.₄₂) 431097 (BaSn₂.₂₀Pb₀.₈₀) and 431098 (SrSn₂.₀₅Pb₀.₉₅), the names of the authors, and citation of the paper (E-mail: crysdata@fiz-karlsruhe.de).

26. Larson, A.C.; Dreele, R.B.V. *General Structure Analysis System (GSAS)*; Los Alamos National Laboratory Report LAUR 86-748; Los Alamos National Laboratory: Los Alamos, NM, USA, 2000.

27. Toby, B.H. EXPGUI, a graphical user interface for GSAS. *J. Appl. Crystallogr.* **2001**, *34*, 210–221. [CrossRef]

28. Schubert, K.; Gauzzi, F.; Frank, K. Kristallstruktur einiger Mg-B3-Phasen. *Z. Metallk.* **1963**, *54*, 422–429.

29. Blaha, P.; Schwarz, K.; Madsen, G.K.H.; Kvasnicka, D.; Luitz, J. *WIEN2K, An Augmented Plane Wave and Local Orbital Program for Calculating Crystal Properties*; TU Wien: Vienna, Austria, 2006; ISBN3-9501031-1-2.

30. Dewhurst, J.K.; Sharma, S.; Nordstrom, L.; Cricchio, F.; Bultmark, F.; Gross, E.K.U. ELK (Vers. 2.1.15), The Elk–FP-LAPW Code. 2013. Available online: http://elk.sourceforge.net (accessed on 5 May 2018).

31. Perdew, J.P.; Burke, S.; Ernzerhof, M. Generalized gradient approximation made simple. *Phys. Rev. Lett.* **1996**, *77*, 3865–3868. [CrossRef] [PubMed]

32. Miller, G.J.; Zhang, Y.; Wagner, F.R. Chemical bonding in solids. In *Handbook of Solid State Chemistry*; Dronskoski, R., Kikkawa, S., Stein, A., Eds.; Wiley-VCH: Weinheim, Germany, 2017; Volume 5, pp. 405–489.

33. Savin, A.; Nesper, R.; Wengert, S.; Fässler, T.F. ELF: The electron localization function. *Angew. Chem. Int. Ed.* **1997**, *36*, 1808–1832. [CrossRef]

34. Kokalj, A. Program XCRYSDEN. *J. Mol. Graph. Model.* **1999**, *17*, 176–178. [CrossRef]

35. Finger, L.W.; Kroeker, M.; Toby, B.H. DRAWXTL: An open-source computer program to produce crystal structure drawings. *J. Appl. Crystallogr.* **2007**, *40*, 188–192. [CrossRef]

36. Bader, R.W.F. *Atoms in Molecules. A Quantum Theory*; International Series of Monographs on Chemistry; Clarendon Press: Oxford, UK, 1994.

37. De-la-Roza, A.O.; Blanco, M.A.; Martá, A.; Pendás, A.M.; Luaña, V. Program CRITIC2 (VERS. 1.0). *Comput. Phys. Commun.* **2009**, *180*, 157–166.

38. De-la-Roza, A.O.; Luaña, V. A fast and accurate algorithm for QTAIM integrations in solids. *J. Comput. Chem.* **2010**, *32*, 291–305. [CrossRef] [PubMed]

39. FIZ Karlsruhe. *Inorganic Crystal Structure Database*; FIZ Karlsruhe: Karlsruhe, Germany, 2017.

40. Cirafici, S.; Franceschi, E. Stacking of close-packed AB_3 layers in RGa_3 compounds (R = heavy rare earth). *J. Less Common Met.* **1981**, *77*, 269–280. [CrossRef]

41. Larson, A.C.; Cromer, D.T.; Stambaugh, C.K. The crystal structure of $PuAl_3$. *Acta Crystallogr.* **1957**, *10*, 443–446. [CrossRef]

42. Shannon, R.D. Revised effective ionic radii and systematic studies of interatomic distances in halides and chalcogenides. *Acta Crystallogr.* **1976**, *A32*, 751–767. [CrossRef]

43. Pearson, W.B. *The Crystal Chemistry and Physics of Metals and Alloys*; Wiley Interscience: Hoboken, NJ, USA, 1972.

44. Wendorff, M.; Röhr, C. Alkaline-earth tri-mercurides $A^{II}Hg_3$ (A^{II}=Ca, Sr, Ba): Binary intermetallic compounds with a common and a new structure type. *Z. Kristallogr.* **2018**, in press.

45. Wade, K. Structural and bonding patterns in cluster chemistry. *Adv. Inorg. Chem. Radiochem.* **1976**, *18*, 1.

46. Jemmis, E.D.; Balakrishnarajan, M.M.; Pancharatna, P.D. Electronic requirements for macropolyhedral boranes. *Chem. Rev.* **2002**, *102*, 93–144. [CrossRef] [PubMed]

47. Todorov, E.; Sevov, S.C. Deltahedral clusters in neat solids: Synthesis and structure of the Zintl phase Cs_4Pb_9 with discrete Pb_9^{4-} clusters. *Inorg. Chem.* **1998**, *37*, 3889–3891. [CrossRef] [PubMed]

48. Fässler, T.F. The renaissance of homoatomic nine-atom polyhedra of the heavier carbon-group element Si-Pb. *Coord. Chem. Rev.* **2001**, *215*, 347–377. [CrossRef]

49. Hoch, C.; Röhr, C.; Wendorff, M. Crystal structure of K_4Sn_9. *Acta Crystallogr.* **2002**, *C58*, 45–46.

50. Bobev, S.; Sevov, S.C. Isolated deltaheral clusters of leadin the solid state: synthesis and characterization of Rb_4Pb_9 and $Cs_{10}K_6Pb_{36}$ with Pb_9^{4-}, and $A'_3A''Pb_4$ (A' = Cs, Rb, K; A'' = Na, Li) with Pb_4^{4-}. *Polyhedron* **2002**, *21*, 641–649. [CrossRef]

51. Fässler, T.F.; Hunziker, M. The nido-Pb_9^{4-} and the Jahn-Teller Distorted closo-Pb_9^{3-} Zintl-Anions: Syntheses, X-ray Structures and Theoretical Studies. *Inorg. Chem.* **1995**, *33*, 5798–5809.

52. Hoch, C.; Wendorff, M.; Röhr, C. Synthesis and Crystal Structure of the Plumbides A_4Pb_9 and the Tetrelides $A_{12}M_{17}$ (A=Na, K, Rb, Cs; M=Si, Ge, Sn). *J. Alloys Compd.* **2003**, *361*, 206–221. [CrossRef]